Rare Met. (2014) 33(4):414–418
DOI 10.1007/s12598-014-0320-5

RARE METALS
www.editorialmanager.com/rmet

Mechanical properties of tungsten heavy alloy and damage behaviors after hypervelocity impact

Zhe Wu*, Yang Zhang, Chun-Mei Yang, Qian-Jun Liu

Received: 24 January 2014 / Revised: 7 May 2014 / Accepted: 16 May 2014 / Published online: 28 June 2014

Abstract 93W-4.5Ni-1.5Fe-1Co (W) was prepared by powder metallurgic method, and then dynamic mechanical properties of this material were tested at high temperature by means of high-temperature split Hopkinson pressure bar (SHPB). The results show that the material possesses high-dynamic mechanical properties, significant temperature effects, and strain hardening behaviors. Used two-stage light gas gun, the penetration test of 93W projectile was finished. After the completion of the test, through the microstructure observation of the residual 93W projectiles with the aid of scanning electron microscopy (SEM) and transmission electron microscopy (TEM), it can be found that there are obvious signs of hot melt existing on the surface of the projectile, a lot of adiabatic shear bands inside the projectile, and microcracks exist at the end of adiabatic shear bands. The test results show that adiabatic shear is the main form to cause the projectile failure and it is the emergence of the adiabatic shearing phenomenon that makes 93W display good self-sharpening property in the process of hypervelocity penetration. At the same time, the results of TEM observation show that there are high-density dislocations at the interface between W and Ni–Fe–Co-based alloy inside the 93W.

Z. Wu*, C.-M. Yang, Q.-J. Liu
College of Mechanical and Electrical Engineering, Northeast Forestry University, Harbin 150040, China
e-mail: wuzhepersonal@126.com

Y. Zhang
College of Science, Northeast Forestry University, Harbin 150040, China

Keywords Tungsten heavy alloy; Dynamic compression; Mechanical properties; Adiabatic shear band

1 Introduction

High-density tungsten alloy was an alloy with tungsten as the matrix and comprising of Ni, Fe, Co, Cu, Mn, Mo, and other elements [1–4]. It is commonly prepared by means of powder metallurgic method and its density can reach 16.5–19.0 $g \cdot cm^{-3}$. The tungsten alloy, possessing a lot of advantages including high strength, high density, small thermal expansion coefficient, anti-oxidation, excellent corrosion resistance property, and good thermal conductivity, can undergo mechanical treatment, weld, forge and press, and heat treatment [5–8]. Owing to these excellent properties, the tungsten alloy is widely used in military and civilian fields [9–12]. At present, the tungsten alloy becomes important materials of manufacturing armor-piercing projectiles and kinetic bullet cores [13]. With advances in launching technology, the launching speed of projectiles increased and the demand to mechanical properties of projectiles was higher, which was required to improve the preparation technology of the tungsten alloy and the strength of the tungsten alloy, and carry out deeper studies on mechanical properties of the tungsten alloy and its damage behaviors after hypervelocity impact [14–17].

To this end, in this paper, the new 93W-4.5Ni-1.5Fe-1Co (93W) prepared by powder metallurgic method was selected to test its dynamic mechanical properties at different temperatures by means of high-temperature split Hopkinson pressure bar (SHPB); meanwhile, the 93W projectile into concrete target test was carried out with two-stage light gas gun, and the microstructures of the

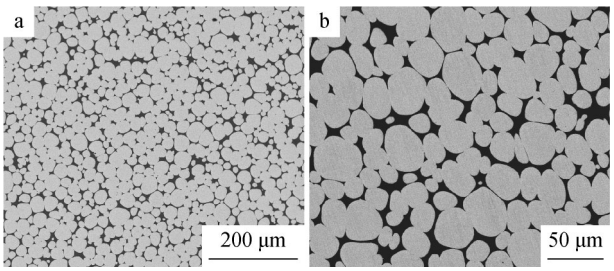

Fig. 1 SEM images of 93W **a** and **b** with different magnifications

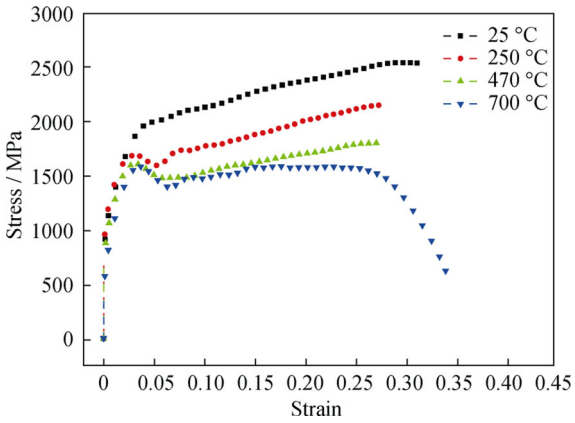

Fig. 2 Dynamic compressive stress–strain curves of 93W at different temperatures

projectile after hypervelocity penetration were observed with the aid of scanning electron microscopy (SEM) and transmission electron microscopy (TEM) to study the microscopic damage behaviors.

2 Experimental

The 93W-4.5Ni-1.5Fe-1Co (93W) was chosen in this experiment. The material was prepared by high-temperature sintering by means of powder metallurgic method after W, Ni, Fe, and Co powders were uniformly mixed. The tungsten particle sizes in the 93W were between 20 and 50 μm. As shown in Fig. 1, the tungsten particles, whose mass fraction accounts for 93 %, are uniformly distributed in the Ni–Fe–Co-based alloy. As can be found from the microstructure observation of the 93W, the 93W is actually composed with W particles as the reinforcement and Ni–Fe-Co-based alloy as the matrix.

Dynamic mechanical tests were finished by means of the high-temperature SHPB device of University of Science and Technology of China. Test samples were cylindrical. Given that the density of the 93W was 2.5 times of that of the pole (martensitic steel), in order to achieve high-strain rate more easily, the sample size was Φ4 mm × 4 mm. Four temperature points (25, 250, 470, and 700 °C) and the compressive strain rate of 4,000 s^{-1} were chosen in this experiment. Each test was finished at least three times to ensure the reliability of the test data.

The hypervelocity penetration into concrete target test was completed by the two-stage light gas gun, and the initial speed of penetration was chosen as 1.8 $km \cdot s^{-1}$. Normal penetration (the projectile and the concrete target formed a right angle) was chosen as the penetration method. The projectile was a 93W flat nosed one with the diameter of 8 mm and the draw ratio of 6:1. After the completion of the penetration, the concrete target should be destroyed to take out the residual projectiles and the projectiles should be soaked and cleaned with alcohol and acetone. Then, the microstructures of the surface and the inside residual projectiles were observed with the aid of SEM and TEM to analyze microscopic damage behaviors of the 93W.

3 Results and discussion

3.1 Mechanical properties of 93W at high temperature

Figure 2 shows the dynamic compression stress–strain curves of the 93W with the strain rate of 4,000 s^{-1} at 25, 250, 470, and 700 °C, respectively. As can be seen from the mechanical curves, the 93W possesses excellent mechanical properties. At 25 °C, the maximum flow stress of the 93W reaches 2,650 MPa; and at 700 °C, the maximum flow stress of the 93W exceeds 1,500 MPa, indicating that the 93W owns excellent high-temperature mechanical properties. As can also be seen from Fig. 2, the test temperature has a great influence on the mechanical properties of the 93W; and with the temperature increasing, the strength of the material decreases gradually. Meanwhile, there exists significant strain hardening phenomena at 25, 250, 470, and 700 °C, respectively; and with the strain increasing, the flow stress of the material increases significantly. However, the stress–strain curve of the material at 700 °C is special. In the initial stage of plastic deformation, the material possesses certain strain hardening behaviors; and with the strain increasing, the flow stress increases. While when the strain reaches 0.15, with the strain increasing, the flow stress begins to decrease slightly; and when the strain reaches 0.27, the stress decreases rapidly and the overall damage of the material occurs, which is caused by the thermal softening and the destruction of the microstructures of the 93W. There are two reasons for the thermal softening of the material: firstly, the

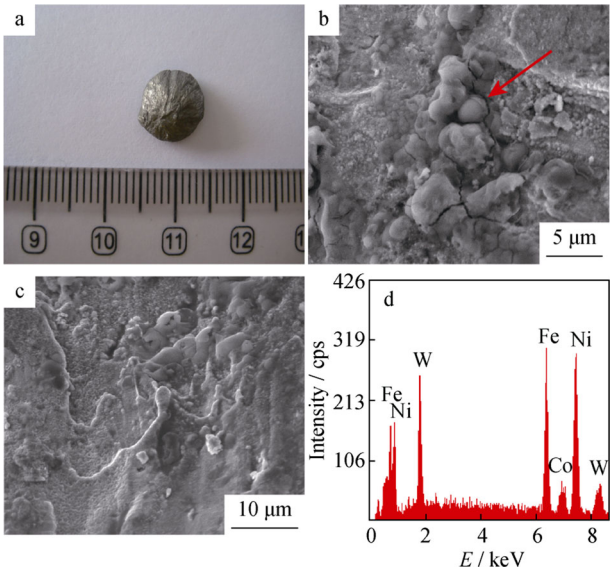

Fig. 3 Observations of exterior of 93W projectile after hypervelocity impact: **a** micro image of whole projectile, **b** SEM image of melt at projectile, **c** SEM image of melt bands at projectile, and **d** EDS result of melt bands in **c**

test temperatures increases; secondly, the high-strain rate compression, belonging to the adiabatic compression, is subject to rapid deformation in a short time; hence, there are large amounts of heat accumulated inside the material, which can not send out and cause the adiabatic temperature to rise. At the same time, the destruction of the material microstructures also has a great influence on the stress–strain curves of the material. In the plastic stage, when the strain reaches 0.15, damages begin to appear inside the samples and with the increase of strain, the internal damages of the material accumulate, which finally causes the overall destruction of the material.

3.2 Damage behaviors of 93W after hypervelocity impact

After the 93W projectile into concrete target test at a speed of 1.8 km·s^{-1} was finished, through tests of length and weight of the residual projectile, it can be found that the length of the projectile reduces significantly and the final length is only 5 mm. Moreover, the mass of the projectile is subject to severe loss and the weighing shows that 90 % mass loss occurs to the projectile. As can be seen from Fig. 3a, the image of the observe side of the warhead of the residual 93W projectile after penetration shows that mushroom-head-shaped warhead does not occur to the 93W projectile after penetration. Through the SEM observation of the warhead, it can be found that there exist a large number of molten alloy beads on the surface of the projectile (as indicated by the arrow in Fig. 3b), and some of them form a molten zone where flowing occurs and then lays on the surface of the projectile after cooling (Fig. 3c), which indicates that in the process of penetration, the warhead is subject to severe impact from the concrete targets. The melt of the 93W at the warhead shows that high temperatures above the material melting point appear at the warhead. Figure 3d is EDS analysis of the melt bands in Fig. 3c, indicating that tungsten, ferrum, nickel, and cobalt are the major elements of the melt bands.

The 93W projectile was cut along the axis, and the microstructures of the projectile after penetration could be observed. Figure 4a and b shows the structure observation of the edge of the warhead. It can be found that owing to the strong impact with the concrete targets, tungsten particles on the edge of the projectile are severely stretched and there are adiabatic shear bands appearing in local areas (as indicated by the arrow in Fig. 4b). The reason is that under the action of high-strain rate, 90 % plastic deformation energy would be converted into heat, and under adiabatic conditions without generating any heat exchange, the concentration of heat generated by the dynamic deformation increases abruptly, so when the softening effects of the material exceed its hardening effects, dramatic deformation occurs to the material and the local adiabatic shear bands would be formed [18–20]. As can be found from Fig. 4c and d, there are adiabatic shear bands appearing in the plastic deformation concentrated areas in the projectile. The emergence of adiabatic shear bands causes the rapid decrease of the material's mechanical properties in this area. With the sustainability of external impact, the shear bands become the fracture origin to produce the initiation of microcracks. From Fig. 4c and d, cracks can be clearly seen at the end of the adiabatic shear bands (as indicated by the arrow in Fig. 4c and d). With the further development of localized deformation, the expansion and connection of microcracks inside the bands would be generated; and finally, the adiabatic shear failure occurs in the projectile, resulting in the rapid release of material in the fracture region from the projectile and making the projectile keep pointed-shaped penetration. Therefore, as shown in Fig. 3a, mushroom-head-shaped warhead does not occur to the 93W projectile after penetration. According to a lot of literatures, when tungsten alloy as the armor-piercing projectile penetrated into metal targets, mushroom-head would occur in the penetration process, thus the penetration ability of the projectile would be reduced [21–23]. While in the test, when the 93W projectile penetrates into concrete targets, mushroom-head-shaped warhead does not occur, and this is not consistent with the result reported in the literatures. The main reason is that the penetration rates of the tungsten alloy projectiles in the literature are mostly less than 1.0 km·s^{-1} and it is difficult

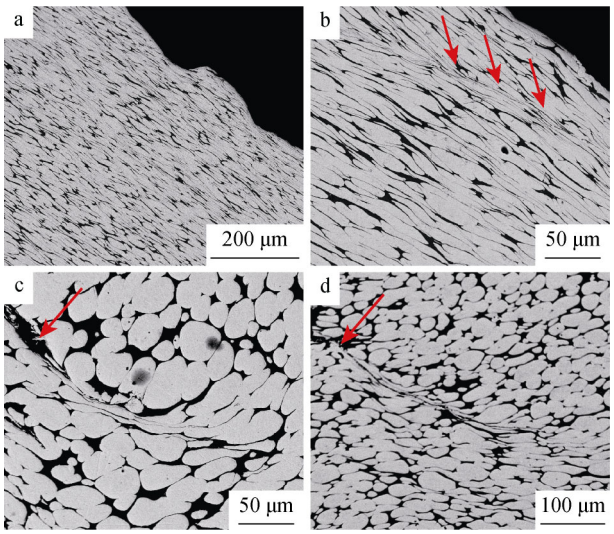

Fig. 4 SEM images of interior of 93W projectile after hypervelocity impact: **a**, **b** damage at edge of projectile and **c**, **d** adiabatic shear bands

for the tungsten alloy to generate adiabatic shear failure at low speeds, then the mushroom-head occurs in the penetration process. While in our test, the penetration rate reaches 1.8 $km \cdot s^{-1}$, and at such a high speed and under the action of high temperature and pressure, the warhead is very prone to thermoplastic instability, which makes the shear deformation occur in a concentrated narrow region; thus, the adiabatic shear bands are generated, the stripping occurs to material in the warhead deformation region, and the mushroom-head-shaped warhead does not appear.

3.3 Change of microstructure of 93W after hypervelocity impact

Figure 5 shows the TEM images of the microstructures of the interface of reinforcement (W) and matrix (Ni–Fe–Co-based alloy). Figure 5a is the image before the 93W penetration. As can be seen, there are certain numbers of dislocations existing at the interface, but the density is not high. The reason for the emergence of dislocations is that during the preparation of the 93W, the thermal expansion coefficient between the matrix alloy and the W particles does not match, resulting in the higher internal stress around the W particles during the process of cooling, thereby forming dislocations [24–26]. Figure 5b is the TEM image of the microstructures of the interface after the 93W penetration. As can be seen, there accumulate high-density dislocations at the W and the matrix alloy interface and there exist serious dislocation entanglement and accumulation especially on the side of the matrix. The

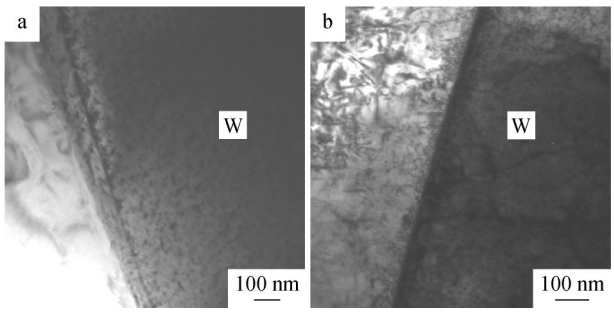

Fig. 5 TEM images of interface of 93W: **a** before impact and **b** after impact

reason for the emergence of large-sized dislocations is that after high velocity impact, the W and the matrix alloy in the 93W would be subject to plastic deformation (Fig. 4a and b), and the dislocation slip is the main mechanism of their plastic deformation; thus, there would be a large number of dislocations. The reason why the dislocation density of the matrix at the interface is higher is that there are many W particles existing in the 93W, which is equivalent to adding many large-scale second-phase particles to the matrix; and as the strength of W is higher than that of the matrix alloy, large numbers of W particles would seriously hinder the dislocation slip in the matrix alloy, and then dislocations in the matrix can only interact with W particles by means of circumvention; thus, there accumulate higher density dislocations in the matrix around W particles.

4 Conclusion

The 93W possesses excellent high-temperature mechanical properties and temperature effect under dynamic impact. The interaction between the 93W projectile and the targets generates adiabatic shear bands inside the material, and the adiabatic shear bands become the fracture origin to produce the initiation of microcracks. With the further development of localized deformation, the expansion and connection of microcracks inside the bands can be generated and finally the adiabatic shear failure occurs in the projectile. Adiabatic shear is the main factor to cause the projectile failure in the process of hypervelocity penetration and it is the emergence of the adiabatic shearing phenomenon that makes the 93W display good self-sharpening property in the process of hypervelocity penetration.

Acknowledgments This study was financially supported by the Fundamental Research Funds for the Central Universities (Nos. DL12C B05 and 2572014EB04-02), the National Natural Science Foundation of China (Nos. 31200434 and 31370566), and the China Postdoctoral Science Foundation (No. 2013M531007).

References

[1] Li R, Chen WG, Wang L. Effects of fiber distribution on density and electrical conductivity of tungsten fiber reinforced Cu-based composite material. Chin J Rare Met. 2013;37(2):243.

[2] Zuo M, Zhang ZS, Teng XY, Geng HR. Refinement of primary Si in Cu-50Si alloys with novel Al-Zr-P master alloy. Rare Met. 2013;32(3):252.

[3] Zhou CS, Yi JH, Luo SD. Sintering high tungsten content W-Ni-Fe heavy alloys by microwave radiation. Metall Trans A. 2014;45(1):455.

[4] Kim EP, Hong MH, Baek WH, Moon IH. The effect of managanese addition on the microstructure of W-Ni-Fe heavy alloy. Metall Trans A. 1999;30(3):627.

[5] Zhu YB, Wang Y, Zhang XY, Qin GW. W-Ni-Fe phase interfacial characteristics of liquid-phase sintered W-Ni-Fe alloy. Int J Refract Metals Hard Mater. 2007;25(4):275.

[6] Conner RD, Dandliker RB, Johnson WL. Mechanical properties of tungsten and steel fiber reinforced $Zr_{41.25}Ti_{13.75}Cu_{12.5}Ni_{10}Be_{22.5}$ metallic glass matrix composites. Acta Mater. 1998;46(17):6089.

[7] Hong SH, Kim BK, Munir ZA. Synthesis and consolidation of nanostructured W-10–40 wt% Cu powders. Mater Sci Eng A. 2005;405(1–2):325.

[8] Ma WF, Kou HC, Chen CS, Li JS, Chang H, Zhou L, Fu HZ. Compressive deformation behaviors of tungsten fiber reinforced Zr-based metallic glass composites. Mater Sci Eng A. 2008;486(1–2):308.

[9] Doré F, Lay S, Eustathopoulos N, Allibert CH. Segregation of Fe during the sintering of doped W-Cu Alloys. Scr Mater. 2003;49(3):237.

[10] Zhou LP, Wang MP, Wang R, Li Z, Zhu JJ, Peng K, Li DY, Li SL. Enhanced adhesion of Cu-W thin films by ion beam assisting bombardment implanting. Trans Nonferrous Met Soc China. 2008;18(2):372.

[11] Yu Y, Wang ED, Hu LX. Effect of nanocrystalline tungsten powders on the microstructure and properties of liquid-phase sintered 93W alloys. Mater Sci and Technol. 2006;14(4):385.

[12] Manel RR, Jan O. Microstructure and texture evolution during the drawing of tungsten wires. Eng Fract Mech. 2009;76(10):1485.

[13] Hong SH, Ryu HJ. Combination of mechanical alloying and two-stage sintering of a 93W-5.6Ni-1.4Fe tungsten heavy alloy. Mater Sci Eng A. 2003;344(1–2):253.

[14] Zou DL, Zhen L, Zhu Y, Xu CY, Shao WZ, Pang BJ. Deformed microstructure evolution in AM60B Mg alloy under hypervelocity impact at a velocity of 5 $km \cdot s^{-1}$. Mater Des. 2010;31(8):3708.

[15] Pappu S, Kennedy C, Murr LE, Magness LS, Kapoor D. Microstructure analysis and comparison of tungsten alloy rod and [001] oriented columnar-grained tungsten rod ballistic penetrators. Mater Sci Eng A. 1999;262(1):115.

[16] Randrianarivony FM, Lair S, Quinones SA, Murr LE. Experimental observations and computer simulations of spherical aluminum-alloy projectiles impacting plane limestone targets. J Mater Sci. 2002;37(24):5197.

[17] Liu JX, Li SK, Fan AL, Sun HC. Effect of fibrous orientation on dynamic mechanical properties and susceptibility to adiabatic shear band of tungsten heavy alloy fabricated through hot-hydrostatic extrusion. Mater Sci Eng A. 2008;487(1–2):235.

[18] Kim HG, Kim KT. Densification behavior of tungsten-fiber-reinforced copper powder compacts under hot isostatic pressing. Int J Mech Sci. 2000;42(7):1339.

[19] Zhang HF, Li H, Wang AM, Fu HM, Ding BZ, Hu ZQ. Synthesis and characteristics of 80 vol% tungsten (W) fibre/Zr based metallic glass composite. Intermetallics. 2009;17(12):1070.

[20] Lins JFC, Sandim HRZ, Kestenbach HJ, Raabe D, Vecchio KS. A microstructural investigation of adiabatic shear bands in an interstitial free steel. Mater Sci Eng A. 2007;457(1–2):205.

[21] Jung SW, Kang SJ, Lee S, Pyokim E, Noh JW, Baek WH. Control of surface carburization and improvement of dynamic fracture behavior in tungsten heavy alloys. Metall Trans A. 2002;33(4):1213.

[22] Qiu KQ, Wang AM, Zhang HF, Ding BZ, Hua ZQ. Mechanical properties of tungsten fiber reinforced ZrAlNiCuSi metallic glass matrix composite. Intermetallics. 2002;10(11–12):1283.

[23] Park S, Kim DK, Lee S, Kim DK, Ryu HJ, Hong SH, Ryu HJ. Dynamic deformation behavior of an oxide-dispersed tungsten heavy alloy fabricated by mechanical alloying. Metall Trans A. 2001;32(8):2011.

[24] Meyers MA, Andrade RU, Chokshi HA. The effect of grain size on the highstrain, high-strain-rate behavior of copper. Metall Mater Trans A. 1995;26:2881.

[25] Zhao D, Ding YG. Simplified nonlinear theory of the dielectric loaded rectangular Cerenkov maser. Chin Phys B. 2012;21(9):094102.

[26] Gu Y, Chao YS, Zhang YH. Soft magnetic properties of amorphous $Fe_{52}Co_{34}Hf_7B_6Cu_1$ alloy treated by pulsed magnetic field and annealing. Chin Phys B. 2012;21(12):127805.